Hongqiang Sang[1]
Advanced Mechatronics Equipment Technology,
Tianjin Area Major Laboratory,
Tianjin Polytechnic University,
Tianjin 300387, China
e-mail: sanghongqiang@tjpu.edu.cn

Reza Monfaredi
The Sheikh Zayed Institute for
Pediatric Surgical Innovation,
Children's National Health System,
Washington, DC 20010
e-mail: rmonfare@childrensnational.org

Emmanuel Wilson
The Sheikh Zayed Institute for
Pediatric Surgical Innovation,
Children's National Health System,
Washington, DC 20010
e-mail: emmanuel.wilson@gmail.com

Hadi Fooladi
The Sheikh Zayed Institute for
Pediatric Surgical Innovation,
Children's National Health System,
Washington, DC 20010
e-mail: HFOOLADIT@childrensnational.org

Diego Preciado
The Sheikh Zayed Institute for
Pediatric Surgical Innovation,
Children's National Health System,
Washington, DC 20010
e-mail: dpreciad@childrensnational.org

Kevin Cleary
The Sheikh Zayed Institute for
Pediatric Surgical Innovation,
Children's National Health System,
Washington, DC 20010
e-mail: KCleary@childrensnational.org

A New Surgical Drill Instrument With Force Sensing and Force Feedback for Robotically Assisted Otologic Surgery

Drilling through bone is a common task during otologic procedures. Currently, the drilling tool is manually held by the surgeon. A robotically assisted surgical drill with force sensing for otologic surgery was developed, and the feasibility of using the da Vinci research kit to hold the drill and provide force feedback for temporal bone drilling was demonstrated in this paper. To accomplish intuitive motion and force feedback, the kinematics and coupling matrices of the slave manipulator were analyzed and a suitable mapping was implemented. Several experiments were completed including trajectory tracking, drill instrument calibration, and temporal bone drilling with force feedback. The results showed that good trajectory tracking performance and minor calibration errors were achieved. In addition, temporal bone drilling could be successfully performed and force feedback from the drill instrument could be felt at the master manipulator. In the future, it may be feasible to use master–slave surgical robotic systems for temporal bone drilling. [DOI: 10.1115/1.4036490]

Keywords: surgical drill instrument, da Vinci research kit, kinematics, force feedback, master–slave control

1 Introduction

Drilling of bone is required in many surgical disciplines such as orthopedic surgery, ear surgery, maxillofacial surgery, and neurosurgery [1]. The critical anatomy within the middle ear, inner ear, and skull base can be accessed by drilling within the temporal bone for commonly performed ontological procedures including acoustic neuroma resection, mastoidectomy, and cochlear implantation, which require high precision and accuracy. As such, the surrounding anatomy and the depth need to be taken into consideration during these procedures. Otherwise, nearby structures surrounding the bone such as veins, arteries, nerves, brain tissue, and spinal cord, may be damaged and cause permanent harm to the patient [2]. Currently, drilling is done using hand-held electric or pneumatic drilling tools. The surgeon controls the speed of the drill by using a pedal or button and manually applies force to the bone to remove material.

One major shortcoming of these hand-held drilling tools is that the surgeon often cannot reliably determine when the proper amount of material has been removed or the desired depth is reached. Due to the inertia of the drilling force, when a breakthrough occurs, the drill bit can be unintentionally pushed further along the drilling axis. In addition, hand physiological tremor of the surgeon may also cause lower accuracy. Therefore, the drilling procedure mainly depends on the surgeon's experience and intuition.

To correct these issues, some researchers have investigated techniques to improve the art of surgical drilling. Some methods focused on depth control and breakthrough detection schemes have been presented [3–11]. To obtain higher precision and accuracy, some robotic devices and systems of different dimensions, complexity, and cost were developed. The Microtable was proposed to accurately guide a drill along a desired straight line trajectory, using a microstereotactic frame attached to bone anchors implanted in the patient's skull [12–15]. A bone-attached parallel kinematic mechanism mounted on a rigid preposition frame was developed to accurately guide the trajectory [16]. A microstereotactic frame as a tool guide was also investigated, which can be

[1]Corresponding author.

Manuscript received September 26, 2016; final manuscript received March 28, 2017; published online June 27, 2017. Assoc. Editor: Venketesh Dubey.

adjusted by a robot [17]. A passive Stewart–Gough platform used as a drill guide in minimally invasive cochlear implantation was proposed. The mechanism can be coupled to bone anchors with spherical heads implanted in a patient's skull [18,19]. A new mechatronic bone drilling tool named DRIBON was developed, which can automatically perform the bone drilling process and efficiently stop when a breakthrough or a layer transition occurs [20]. An automatic drill guide was developed, which could fit within a current minimally invasive cochlear implant surgical system and also provide a method for measuring temperature rise at the facial nerve [21].

A robotic system for lateral skull based surgery was developed based on a table-mounted robotic arm and a force/torque (F/T) sensor [22], which integrated an optical tracking system, an image-guidance system, a head fixation system, and a touch screen interface. The results showed that the system was promising, however, it depended on the tracking system and the errors related to monitoring and aligning the patient with the robot. To eliminate this limitation, a compact, bone-attached, and computed tomography (CT) image-guided robot was developed for temporal bone milling, which was attached to the patient by three titanium spheres on a preposition frame [23]. Phantom results showed that the system was accurate and there was no overlap between the experimentally removed volume and the critical structures. A Mitsubishi RV-3S industrial robot with an infrared tracking system and bone-implanted markers was used for autonomous percutaneous placement of a cochlear implant in a cadaveric model [24]. Results showed that the system was accurate and reliable, however, its performance relied on the registration accuracy level. A telerobotic system was developed, which included a Phantom Omni (SensAble Technologies, Inc., Cambridge, MA) master robot and a cable transmission mechanism slave robot [25]. The prototype was tested in human temporal bone specimens. The results showed that otologists could successfully place the piston prosthesis in the stapedotomy in both velocity/position and position/position command modes. A compact, bone-attached robot with four degrees-of-freedom (DOFs) was used for the mastoidectomy portion of the surgery. The target volume to be removed can be manually identified by the surgeon pre-operatively in a CT scan and converted to a milling path for the robot [26]. A complete review of hand-held manipulators was done, and the emerging technical trends in hand-held medical robots and future development opportunities for promoting their wider clinical uptake are presented in Ref. [27].

A cadaveric feasibility study was performed using the da Vinci system for cochlear implantation [28]. An attachment was developed to attach a powered drill to one of the arms, and an augmented reality capability was incorporated into the surgeon's view, through segmentation of cone-beam high-resolution CT scans of the temporal bones. Surgery was completed successfully in two bones. However, three limitations were reported. First, as existing devices used in the procedure such as the suction irrigator are too large, a smaller profile-articulating suction-irrigation device for navigation in the facial recess is necessary. Second, it was found necessary to improve the magnification of the 3D endoscope for improved visualization through the posterior tympanostomy. Third, to adequately define the accuracy, precision, and feasibility of the system, more cadaveric specimens need to be completed by this approach. In addition, there was no force feedback.

Compared to hand-held instruments or robots, master–slave robots or cooperative robots can possibly achieve better accuracy and precision. Master–slave surgical robotic systems like the da Vinci surgical system have the advantages of 3D surgical vision, motion scaling, fine motion, hand–eye coordination, and hand tremor reduction, which has achieved significant development in recent years and has been applied in many surgical procedures, such as urologic surgery, general laparoscopic surgery, gynecologic laparoscopic surgery, and cardiac surgery [29,30]. In this paper, the research based on the da Vinci research kit (dVRK)

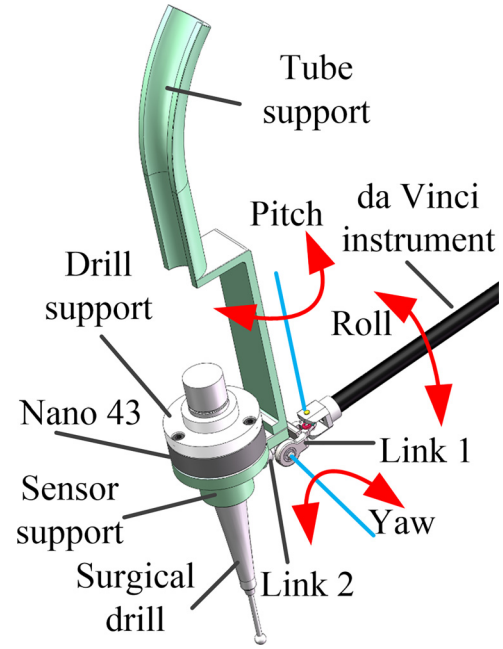

Fig. 1 The 3DOF tendon-driven surgical instrument

donated by Intuitive Surgical, Inc., (Sunnyvale, CA) was performed to investigate the feasibility of using a master–slave surgical robotic system to accomplish surgical drilling with force sensing and force feedback for otology procedures.

2 Design of the Surgical Drill Instrument

To adapt to the sterile adapter of patient side manipulators (PSMs), a 3DOF tendon-driven surgical drill instrument was designed on the basis of a da Vinci surgical instrument, which integrated a Nano43 F/T sensor produced by ATI Industrial Automation (Apex, NC) and a Hall Osteon drill produced by Linvatec Corporation (Albany, NY), which is shown in Fig. 1. Except for self-roll motion about the axis of the surgical drill, the surgical drill instrument can provide 3DOF motion including pitch, yaw, and roll DOFs, and force and torque sensing capability. These DOFs of the instrument are actuated by a tendon–pulley system and DC servo motors. The ranges of the roll motion, the pitch motion, and the yaw motion are all from −90 deg to 90 deg.

The layout design of the tendon transmission is shown in Fig. 2. The roll DOF can be provided by the modified Da Vinci instrument. Link 1 and the driven pulley for pitch and link 2 and the driven pulley for yaw are fitted together, respectively. The tendons s_1 and s_2 can drive the driven pulley for pitch to rotate around the pitch axis, which can accomplish the pitch DOF. The tendons s_3 and s_4 can drive the driven pulley for yaw to rotate around the yaw axis, which can accomplish the yaw DOF.

The interface design of the surgical drill with the F/T sensor is shown in Fig. 3. The sensor support and the mounting adapter

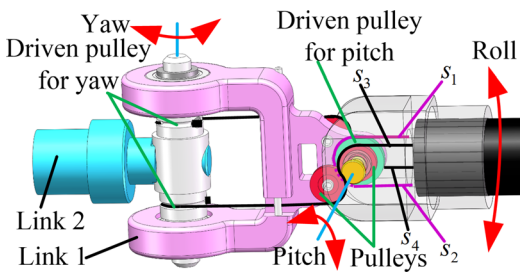

Fig. 2 The layout design of the tendon transmission

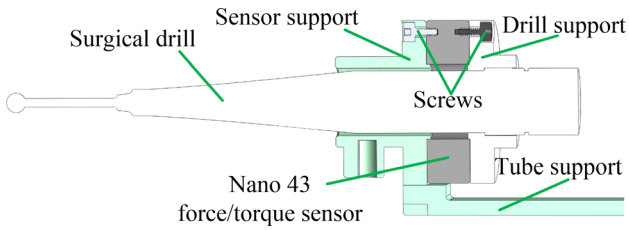

Fig. 3 The interface design of the surgical drill with F/T sensor

plate of the F/T sensor are connected by three screws. The drill support and the tool adapter plate of the F/T sensor are connected by three screws. The drill and the drill support are connected by a set screw. The tube support and the sensor support are fitted together. The tube support is used to fasten the hose of the Hall Osteon drill and the electric cable of the F/T sensor, which can ensure that the measured values of the F/T sensor are not affected by them.

3 Forward Kinematics and Coupling Matrices of the PSM1

To accomplish master–slave intuitive motion control, decoupled control of the surgical drill instrument and F/T information transformation, Denavit–Hartenberg (DH) parameters, kinematics, tooltip-offset transform matrix, and coupling matrices of the PSM1 are analyzed and provided for the dVRK.

3.1 Forward Kinematics. Frames of the PSM1 are assigned to each link according to the modified DH convention. Figure 4 shows the coordinate frame assignment of the PSM1 and our surgical drill instrument.

The origins O_0, O_1, and O_2 of coordinate frames 0, 1, and 2 are located at the remote center of motion (RCM), and the origins O_4 and O_5 of coordinate frames 4 and 5 and the origins O_7 and O_8 of coordinate frames 7 and 8 are coincident, respectively. The coordinate frame 8 is assigned to the control point of the surgical drill instrument. The coordinate frame of the Nano43 F/T sensor is the

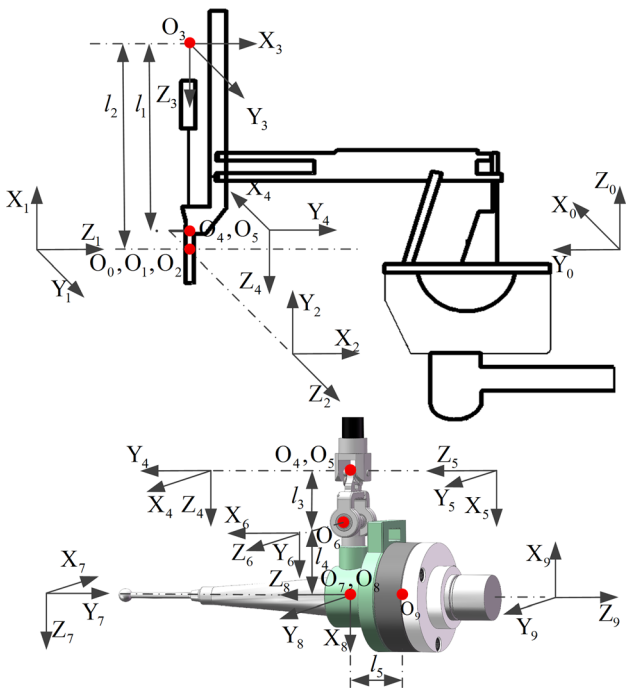

Fig. 4 The coordinate frame assignment of the PSM1

Table 1 The modified DH parameters of the PSM1

Frame i	α_{i-1}	a_{i-1}	d_i	θ_i
1	$\pi/2$	0	0	$\theta_1 + (\pi/2)$
2	$-\pi/2$	0	0	$\theta_2 - (\pi/2)$
3	$\pi/2$	0	$d_3 - l_2$	0
4	0	0	l_1	$\theta_4 - (\pi/2)$
5	$-\pi/2$	0	0	$\theta_5 - (\pi/2)$
6	$-\pi/2$	l_3	0	$\theta_6 - (\pi/2)$
7	$-\pi/2$	0	l_4	$\pi/2$
8	$\pi/2$	0	0	$\pi/2$
9	π	0	l_5	π

Note: $\theta_i (i = 1, 2, 4, 5, 6)$ and d_3 are the corresponding joint variables.

coordinate frame 9. The modified DH parameters of the PSM1 are given in Table 1.

The forward kinematics of the PSM1 with the surgical drill instrument can be obtained by

$$ {}^0\mathbf{T}_8 = {}^0\mathbf{T}_1\,{}^1\mathbf{T}_2\,{}^2\mathbf{T}_3\,{}^3\mathbf{T}_4\,{}^4\mathbf{T}_5\,{}^5\mathbf{T}_6\,{}^6\mathbf{T}_7\,{}^7\mathbf{T}_8 \tag{1} $$

where ${}^j\mathbf{T}_i (i = 1, 2, \ldots, 8; j = 0, 1, \ldots, 7)$ is a transformation that relates frame i to frame j.

The tooltip-offset transform matrix can be obtained by

$$ {}^6\mathbf{T}_8 = {}^6\mathbf{T}_7\,{}^7\mathbf{T}_8 = \begin{bmatrix} 0 & 0 & 1 & 0 \\ 1 & 0 & 0 & l_4 \\ 0 & 1 & 0 & 0 \\ 0 & 0 & 0 & 1 \end{bmatrix} \tag{2} $$

3.2 Coupling Matrices. The transmission schematic of the 3DOF tendon-driven surgical drill instrument is shown in Fig. 5, where r_i $(i = 1, 2, \ldots, 6)$ and $r_{\text{disk}i} (i = 1, 2, 3)$ are the radii of the pulleys and the disks, respectively, and $\theta_i (i = 4, 5, 6)$ and $\theta_{\text{disk}i} (i = 1, 2, 3)$ are the joint angular displacements and the driven disk angular displacements, respectively.

According to the tendon movement displacement equality, the relationship between the joint angular displacements and the driven disk angular displacements can be described as

$$ \mathbf{A}\boldsymbol{\theta}_{\text{joint}} = \mathbf{R}_{\text{disk}}\boldsymbol{\theta}_{\text{disk}} \tag{3} $$

where $\mathbf{A} = \begin{bmatrix} r_1 & 0 & 0 \\ 0 & r_2 & 0 \\ 0 & r_3 & r_6 \end{bmatrix}$, $\boldsymbol{\theta}_{\text{joint}} = \begin{bmatrix} \theta_4 \\ \theta_5 \\ \theta_6 \end{bmatrix}$, $\mathbf{R}_{\text{disk}} = \begin{bmatrix} r_{\text{disk1}} & 0 & 0 \\ 0 & r_{\text{disk2}} & 0 \\ 0 & 0 & r_{\text{disk3}} \end{bmatrix}$, and $\boldsymbol{\theta}_{\text{disk}} = \begin{bmatrix} \theta_{\text{disk1}} \\ \theta_{\text{disk2}} \\ \theta_{\text{disk3}} \end{bmatrix}$.

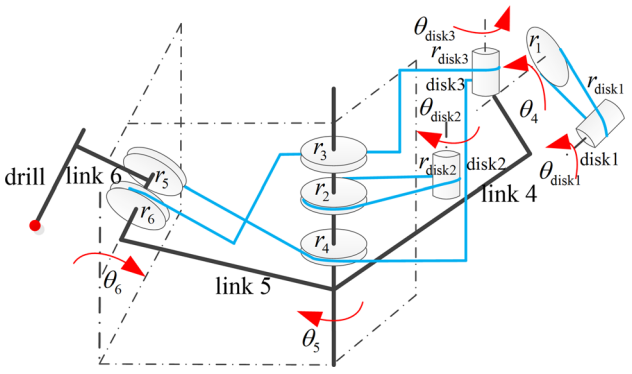

Fig. 5 The transmission schematic of the 3DOF tendon-driven surgical drill instrument

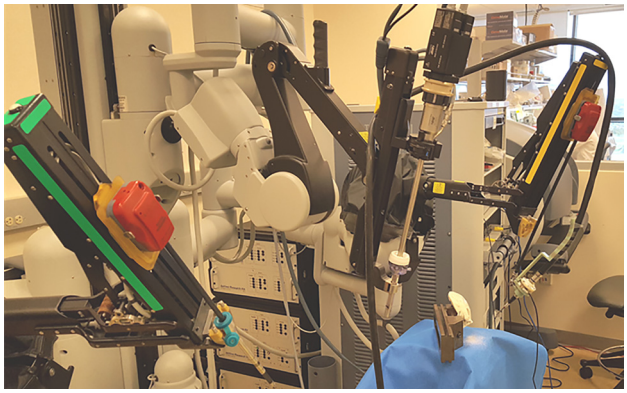

Fig. 6 The master–slave surgical drill robotic system based on the dVRK

Using Eq. (3) and considering the work done on the rotating joint, the position coupling matrices $\mathbf{M}_{j2dp}$ from the joint to the disk and $\mathbf{M}_{d2jp}$ from the disk to the joint and the torque coupling matrices $\mathbf{M}_{d2jt}$ from the disk to the joint and $\mathbf{M}_{j2dt}$ from the joint to the disk can be obtained as

$$\mathbf{M}_{j2dp} = \mathbf{M}_{d2jt}^{T} = \begin{bmatrix} \frac{r_1}{r_{disk1}} & 0 & 0 \\ 0 & \frac{r_2}{r_{disk2}} & 0 \\ 0 & \frac{r_3}{r_{disk3}} & \frac{r_6}{r_{disk3}} \end{bmatrix},$$

$$\mathbf{M}_{d2jp} = \mathbf{M}_{j2dt}^{T} = \begin{bmatrix} \frac{r_{disk1}}{r_1} & 0 & 0 \\ 0 & \frac{r_{disk2}}{r_2} & 0 \\ 0 & -\frac{r_{disk2} r_3}{r_2 r_6} & \frac{r_{disk3}}{r_6} \end{bmatrix} \tag{4}$$

4 Master–Slave Motion and Force Feedback Control

The master–slave surgical drill robotic system based on the dVRK is shown in Fig. 6, which includes the first generation da Vinci surgical robot system, control system that was developed by Johns Hopkins University, Baltimore, MD and Worcester Polytechnic Institute, Worcester, MA [31,32], and the designed surgical drill instrument.

The current master–slave motion and force feedback control structure is shown in Fig. 7. The positions (rotation/translation) calculated by kinematics from the master tool manipulator right (MTMR) manipulated by a human operator are sent to the PSM1 through the mapping transformation and the position scaling factor K_p. The environment forces measured by the Nano43 F/T sensor installed at the surgical drill instrument of the PSM1 are fed back to the MTMR through the force and torque transformation and the force scaling factor K_f. Force feedback can be implemented by the joint torques obtained by using the environment force and transpose of the Jacobian matrix of the MTMR. The PSM1 uses a local proportional–integral–derivative (PID) controller for each joint to ensure position/velocity tracking.

4.1 The Master–Slave Motion Control. Motion scaling allows a large MTMR motion to correspond to a small PSM1 motion and can make the PSM1 steady even under jerky MTMR movements. To accomplish intuitive motion control, the visual image of the control point motion of the PSM1 on the monitor must be aligned with the motion of the MTMR operated by the surgeon.

The required rotation matrix can be expressed as

$$\begin{aligned} {}^{PSM1_{base}}\mathbf{R}_{MTMR_{base}} = {}^{PSM1_{base}}\mathbf{R}_{world}\, {}^{world}\mathbf{R}_{ECM_{base}}\, {}^{ECM_{base}}\mathbf{R}_{ECM_{tcpE}} \\ \times {}^{ECM_{tcpE}}\mathbf{R}_{monitor}\, {}^{monitor}\mathbf{R}_{MTMR_{base}} \end{aligned} \tag{5}$$

where $MTMR_{base}$, $PSM1_{base}$, ECM_{base}, monitor, ECM_{tcpE}, and world are the base coordinate frame of the MTMR, the base coordinate frame of the PSM1, the base coordinate frame of the endoscopic camera manipulator (ECM), the monitor coordinate frame, the control point coordinate frame of the ECM, and the world coordinate frame, respectively.

It can be seen from Eq. (5), the rotation matrix only changes when the ECM is moved, because ${}^{PSM1_{base}}\mathbf{R}_{world}$ and ${}^{monitor}\mathbf{R}_{MTMR_{base}}$ are between fixed frames. When the master and slave base coordinate frames are only considered, the rotation matrix can be calculated as

$${}^{PSM1_{base}}\mathbf{R}_{MTMR_{base}} = {}^{PSM1_{base}}\mathbf{R}_{world}\, {}^{world}\mathbf{R}_{MTMR_{base}} = \begin{bmatrix} -1 & 0 & 0 \\ 0 & -1 & 0 \\ 0 & 0 & 1 \end{bmatrix} \tag{6}$$

The position and the orientation of the MTMR are transformed into the base coordinate frame of the PSM1, which can be described as

$$\begin{aligned} {}^{PSM1_{base}}\mathbf{T}_{MTMR_{tcp}} &= \begin{bmatrix} {}^{PSM1_{base}}\mathbf{R}_{MTMR_{base}} & 0 \\ 0 & 1 \end{bmatrix} {}^{MTMR_{base}}\mathbf{T}_{MTMR_{tcp}} \\ &= \begin{bmatrix} {}^{PSM1_{base}}\mathbf{R}_{MTMR_{base}} & 0 \\ 0 & 1 \end{bmatrix} \begin{bmatrix} {}^{MTMR_{base}}\mathbf{R}_{MTMR_{tcp}} & K_p \cdot [\Delta x \;\; \Delta y \;\; \Delta z]^{T} \\ 0 & 1 \end{bmatrix} \end{aligned} \tag{7}$$

The desired tool control point of the PSM1 in its base coordinate frame can be described as

$$\begin{aligned} {}^{PSM1_{base}}\mathbf{T}_{PSM1_{tcp}(desired)}(i) \\ = \mathbf{g}\left({}^{PSM1_{base}}\mathbf{T}_{PSM1_{tcp}}(i-1),\; {}^{PSM1_{base}}\mathbf{T}_{MTMR_{tcp}}(i),\; \text{couple}(i) \right) \end{aligned} \tag{8}$$

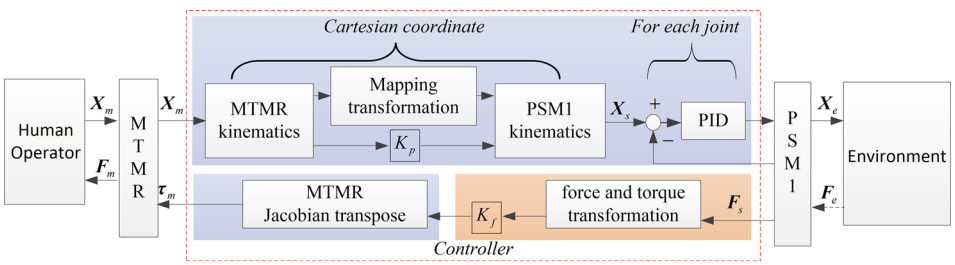

Fig. 7 The master–slave motion and force feedback control structure

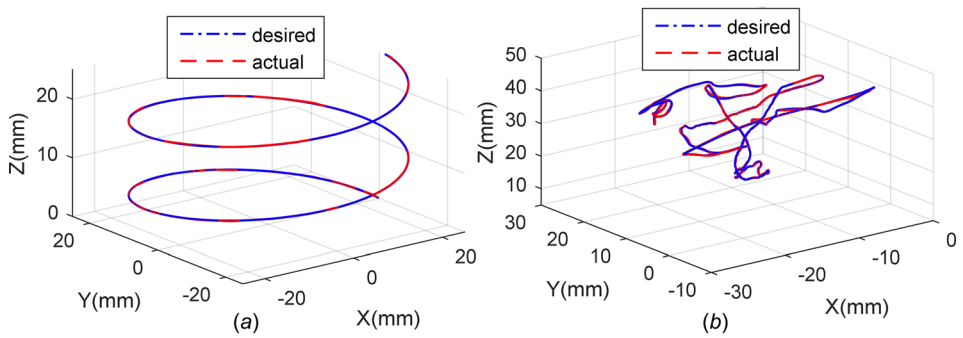

Fig. 8 The trajectory tracking responses under two modes: (*a*) command mode and (*b*) master–slave mode

where $\mathbf{g}(\cdot)$ is a function of ${}^{\mathrm{PSM1}_{\mathrm{base}}}\mathbf{T}_{\mathrm{PSM1}_{\mathrm{tcp}}}(i-1)$, ${}^{\mathrm{PSM1}_{\mathrm{base}}}\mathbf{T}_{\mathrm{MTMR}_{\mathrm{tcp}}}(i)$, and couple($i$). The couple($i$) is a Boolean flag that indicates whether or not the MTMR and the PSM1 are coupled. If the MTMR and the PSM1 are coupled, then couple(i) = True; otherwise, couple(i) = False. $i-1$ and i are the $i-1$th and ith time steps.

When the PSM1 is coupled to the MTMR, the PSM1 follows the motion of the MTMR with position scaling factor. The desired tool control point of the PSM1 ${}^{\mathrm{PSM1}_{\mathrm{base}}}\mathbf{T}_{\mathrm{PSM1}_{\mathrm{tcp}}(\mathrm{desired})}$ is sent to the inverse kinematics of the PSM1 and transformed into corresponding joint angles.

4.2 The Force/Torque Transformation. The Nano43 F/T sensor attached to the surgical drill instrument measures not only the contact force and torque of the environment exerted on the surgical drill but also the noncontact forces caused by the gravitational and inertial effects as well as linear bias. Therefore, the force and the torque measured by the F/T sensor can be calculated as

$$\begin{bmatrix}\mathbf{F}_{\mathrm{S}}\\ \boldsymbol{\tau}_{\mathrm{S}}\end{bmatrix}=\begin{bmatrix}\mathbf{F}_{\mathrm{E}}\\ \boldsymbol{\tau}_{\mathrm{E}}\end{bmatrix}+\begin{bmatrix}\mathbf{F}_{\mathrm{G}}\\ \boldsymbol{\tau}_{\mathrm{G}}\end{bmatrix}+\begin{bmatrix}\mathbf{F}_{\mathrm{I}}\\ \boldsymbol{\tau}_{\mathrm{I}}\end{bmatrix}+\begin{bmatrix}\mathbf{F}_{\mathrm{O}}\\ \boldsymbol{\tau}_{\mathrm{O}}\end{bmatrix} \tag{9}$$

where $\mathbf{F}_{\mathrm{S}}$ and $\boldsymbol{\tau}_{\mathrm{S}}$ are the force and torque measured by the F/T sensor, $\mathbf{F}_{\mathrm{E}}$ and $\boldsymbol{\tau}_{\mathrm{E}}$ are the force and torque of the environment exerted on the surgical drill, $\mathbf{F}_{\mathrm{G}}$ and $\boldsymbol{\tau}_{\mathrm{G}}$ are the force and torque caused by gravity, $\mathbf{F}_{\mathrm{I}}$ and $\boldsymbol{\tau}_{\mathrm{I}}$ are the inertial force and torque produced by the surgical drill dynamics, and $\mathbf{F}_{\mathrm{O}}$ and $\boldsymbol{\tau}_{\mathrm{O}}$ are the linear force and torque offsets.

The contact force and torque need to be distinguished from the F/T sensor measurement and the effects of the noncontact force and torque need to be eliminated. As the PSM1 with the surgical drill instrument is manipulated at a very low speed, the surgical drill dynamic effect will be neglected here. When the surgical drill moves freely in the workspace of the PSM1, Eq. (9) can be expressed as

$$\begin{bmatrix}\mathbf{F}_{\mathrm{S}}\\ \boldsymbol{\tau}_{\mathrm{S}}\end{bmatrix}=\begin{bmatrix}\mathbf{F}_{\mathrm{G}}\\ \boldsymbol{\tau}_{\mathrm{G}}\end{bmatrix}+\begin{bmatrix}\mathbf{F}_{\mathrm{O}}\\ \boldsymbol{\tau}_{\mathrm{O}}\end{bmatrix} \tag{10}$$

The force $\mathbf{F}_{\mathrm{G}}$ affecting the measurement of the F/T sensor can be calculated by

$$\mathbf{F}_{\mathrm{G}}=m\mathbf{g}_s=m\mathbf{R}(\mathbf{q})\mathbf{g} \tag{11}$$

where $\mathbf{F}_{\mathrm{G}}=[F_{\mathrm{x}}\quad F_{\mathrm{y}}\quad F_{\mathrm{z}}]^{\mathrm{T}}$ is the gravity vector, m is the mass of the surgical drill, $\mathbf{g}=[0\quad 0\quad -\mathrm{g}]^{\mathrm{T}}$ is the acceleration of gravity vector described in the coordinate frame 0 of the PSM1, and $\mathbf{g}_s=\mathbf{R}(\mathbf{q})\mathbf{g}$ is the description of gravity vector in the F/T sensor coordinate frame, where $\mathbf{R}(\mathbf{q})=[r_{ij}](i,j=1,2,3)$ is the rotation matrix of the F/T sensor in the coordinate frame 0 of the PSM1.

Similarly, the torque $\boldsymbol{\tau}_{\mathrm{G}}$ affecting measurement of the F/T sensor can be calculated by

$$\boldsymbol{\tau}_{\mathrm{G}}=m\mathbf{r}_{\mathrm{sd}}\mathbf{g}_s=m\mathbf{r}_{\mathrm{sd}}\mathbf{R}(\mathbf{q})\mathbf{g} \tag{12}$$

where $\boldsymbol{\tau}_{\mathrm{G}}=[\tau_{\mathrm{x}}\quad \tau_{\mathrm{y}}\quad \tau_{\mathrm{z}}]^{\mathrm{T}}$ is the gravity torque vector, and $\mathbf{r}_{\mathrm{sd}}=[r_{\mathrm{x}}\quad r_{\mathrm{y}}\quad r_{\mathrm{z}}]^{\mathrm{T}}$ is the vector from the origin O_9 of the F/T sensor to the centroid of the surgical drill.

Combining Eq. (10) with Eqs. (11) and (12) yields

$$\begin{aligned}\begin{bmatrix}\mathbf{F}_{\mathrm{G}}\\ \boldsymbol{\tau}_{\mathrm{G}}\end{bmatrix}&=\begin{bmatrix}\mathbf{F}_{\mathrm{S}}\\ \boldsymbol{\tau}_{\mathrm{S}}\end{bmatrix}-\begin{bmatrix}\mathbf{F}_{\mathrm{O}}\\ \boldsymbol{\tau}_{\mathrm{O}}\end{bmatrix}=\begin{bmatrix}F_{\mathrm{sx}}\\ F_{\mathrm{sy}}\\ F_{\mathrm{sz}}\\ \tau_{\mathrm{sx}}\\ \tau_{\mathrm{sy}}\\ \tau_{\mathrm{sz}}\end{bmatrix}-\begin{bmatrix}F_{\mathrm{ox}}\\ F_{\mathrm{oy}}\\ F_{\mathrm{oz}}\\ \tau_{\mathrm{ox}}\\ \tau_{\mathrm{oy}}\\ \tau_{\mathrm{oz}}\end{bmatrix}\\ &=m\begin{bmatrix}1&0&0\\ 0&1&0\\ 0&0&1\\ 0&-r_z&r_y\\ r_z&0&-r_x\\ -r_y&r_x&0\end{bmatrix}\mathbf{R}(\mathbf{q})\mathbf{g}\end{aligned} \tag{13}$$

Equation (13) includes ten unknown parameters: the offset values of force and torque, the centroid position, and the mass of the surgical drill. According to Eq. (13), Eqs. (14) and (15) can be obtained as

$$\mathbf{Y}_{\mathrm{F}}\mathbf{X}_{\mathrm{F}}=\mathbf{F}_{\mathrm{s}} \tag{14}$$

where $\mathbf{Y}_{\mathrm{F}}=\begin{bmatrix}1&0&0&-r_{13}\mathrm{g}\\ 0&1&0&-r_{23}\mathrm{g}\\ 0&0&1&-r_{33}\mathrm{g}\end{bmatrix}$ and $\mathbf{X}_{\mathrm{F}}=\begin{bmatrix}F_{\mathrm{ox}}&F_{\mathrm{oy}}&F_{\mathrm{oz}}&m\end{bmatrix}^{\mathrm{T}}$.

$$\mathbf{Y}_{\tau}\mathbf{X}_{\tau}=\boldsymbol{\tau}_{\mathrm{S}} \tag{15}$$

where $\mathbf{Y}_{\tau}=\begin{bmatrix}1&0&0&0&-r_{33}mg&r_{23}mg\\ 0&1&0&r_{33}mg&0&-r_{13}mg\\ 0&0&1&-r_{23}mg&r_{13}mg&0\end{bmatrix}$ and $\mathbf{X}_{\tau}=\begin{bmatrix}\tau_{\mathrm{ox}}&\tau_{\mathrm{oy}}&\tau_{\mathrm{oz}}&\mathrm{r_x}&\mathrm{r_y}&\mathrm{r_z}\end{bmatrix}^{\mathrm{T}}$.

According to Eq. (9), the force $\mathbf{F}_{\mathrm{E}}$ and the torque $\boldsymbol{\tau}_{\mathrm{E}}$ of the environment exerted on the surgical drill instrument can be obtained as

$$\begin{bmatrix}\mathbf{F}_{\mathrm{E}}\\ \boldsymbol{\tau}_{\mathrm{E}}\end{bmatrix}=\begin{bmatrix}\mathbf{F}_{\mathrm{S}}\\ \boldsymbol{\tau}_{\mathrm{S}}\end{bmatrix}-\begin{bmatrix}\mathbf{F}_{\mathrm{G}}\\ \boldsymbol{\tau}_{\mathrm{G}}\end{bmatrix}-\begin{bmatrix}\mathbf{F}_{\mathrm{O}}\\ \boldsymbol{\tau}_{\mathrm{O}}\end{bmatrix} \tag{16}$$

The force $\mathbf{F}_{\mathrm{E}}$ and the torque $\boldsymbol{\tau}_{\mathrm{E}}$ exerted on the surgical drill in the coordinate frame 8 can be described as

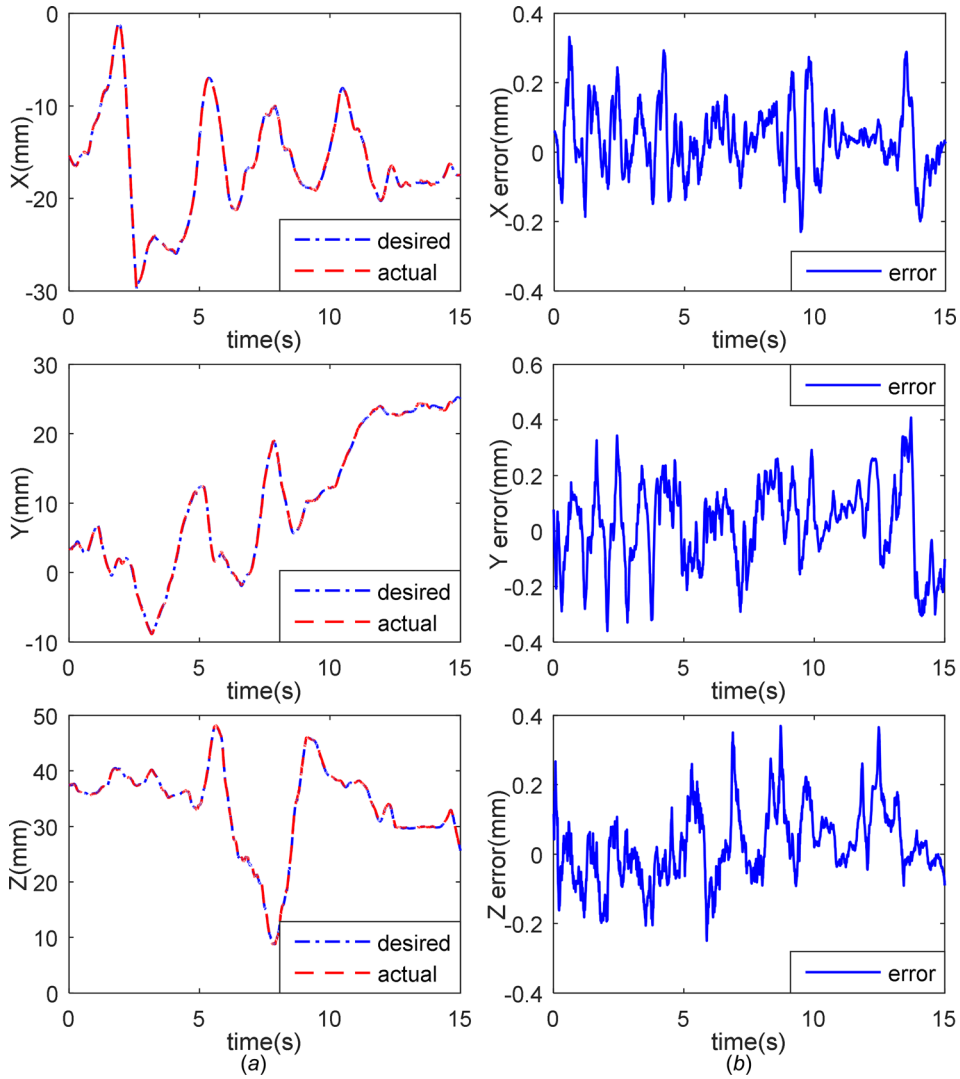

Fig. 9 The trajectory tracking responses and tracking errors: (*a*) trajectory tracking and (*b*) tracking errors

$$\begin{bmatrix} {}^{8}\mathbf{F}_{9} \\ {}^{8}\boldsymbol{\tau}_{9} \end{bmatrix} = \begin{bmatrix} {}^{8}\mathbf{R}_{9}^{\mathrm{T}} & 0 \\ -{}^{8}\mathbf{R}_{9}^{\mathrm{T}}\hat{\mathbf{p}}_{98} & {}^{8}\mathbf{R}_{9}^{\mathrm{T}} \end{bmatrix} \begin{bmatrix} \mathbf{F}_{\mathrm{E}} \\ \boldsymbol{\tau}_{\mathrm{E}} \end{bmatrix} \tag{17}$$

where ${}^{8}\mathbf{R}_{9}^{\mathrm{T}} = \begin{bmatrix} -1 & 0 & 0 \\ 0 & 1 & 0 \\ 0 & 0 & -1 \end{bmatrix}$, $\hat{\mathbf{p}}_{98} = \begin{bmatrix} 0 & l_5 & 0 \\ -l_5 & 0 & 0 \\ 0 & 0 & 0 \end{bmatrix}$, and $\mathbf{p}_{98} = \begin{bmatrix} 0 \\ 0 \\ -l_5 \end{bmatrix}$.

4.3 The Implementation of Drilling Force Feedback. The wrench $\mathbf{w}_{\mathrm{PSM1_{tcp}}}$ of the tool control point of the PSM1 is fed back to the MTMR which generates the same magnitude forces at the tool control point of the MTMR to accomplish the force feedback.

The wrench transformation ${}^{\mathrm{MTMR_{tcp}}}\mathbf{w}_{\mathrm{PSM1_{tcp}}}$ from the control point of the PSM1 to the control point of the MTMR using the body wrench can be expressed as

$${}^{\mathrm{MTMR_{tcp}}}\mathbf{w}_{\mathrm{PSM1_{tcp}}} = \begin{bmatrix} {}^{\mathrm{PSM1_{tcp}}}\mathbf{R}_{\mathrm{MTMR_{tcp}}}^{\mathrm{T}} & 0 \\ 0 & {}^{\mathrm{PSM1_{tcp}}}\mathbf{R}_{\mathrm{MTMR_{tcp}}}^{\mathrm{T}} \end{bmatrix} \mathbf{w}_{\mathrm{PSM1_{tcp}}} \tag{18}$$

Given the joint torque $\boldsymbol{\tau}$, the desired body wrench applied at the tool control point of the MTMR can be obtained by

$${}^{\mathrm{MTMR_{tcp}}}\mathbf{w}_{\mathrm{PSM1_{tcp}}} = (\mathbf{J}_b^{\mathrm{T}})^{+}\boldsymbol{\tau} \tag{19}$$

where $(\mathbf{J}_b^{\mathrm{T}})^{+}$ is the generalized inverse matrix of the body Jacobian transpose matrix of the MTMR.

5 Experiments and Results

Several experiments were completed to verify the feasibility of using the newly developed tool with the da Vinci robotic system.

5.1 The Trajectory Tracking Experiments. To verify the validity of the PSM1 kinematics, the trajectory tracking experiment under command mode was performed. The actual trajectory of the PSM1 in Cartesian space was measured by the Certus HD optical tracking system (Northern Digital, Inc., Waterloo, ON). Six active markers were used to build a rigid body. The rigid body was attached to the robot base. Another active marker was attached to the tip of the tool. The tool tip motion with respect to robot base can be measured by using the rigid frame and defining new coordinate frame. The desired command trajectory was designed and described as

Table 2 Trajectory tracking errors of the PSM1

	X (mm)	Y (mm)	Z (mm)	Space (mm)
RMS	0.1008	0.1482	0.1055	0.2080
MAX	0.3320	0.4084	0.3696	0.4441

$$\begin{cases} X = 25\cos(n) \\ Y = 25\sin(n), \quad n \in [0, 4\pi] \\ Z = 2n \end{cases} \tag{20}$$

To prove the correctness of the master–slave motion control, the trajectory tracking experiment under master–slave mode was performed with master–slave 1:1 scaling factor. An operator held the MTMR to produce a random space trajectory as the desired trajectory, and the actual trajectory of the PSM1 in Cartesian space was measured by the optical tracking system. Figure 8 gives the trajectory tracking responses under command mode and master–slave mode.

It can be seen that the actual trajectory perfectly coincides with the desired trajectory under command mode, which shows that the kinematics of the PSM1 with the surgical drill instrument and the tendon transmission schematic are correct, and the tension of the tendon is fine. The actual trajectory almost coincides with the desired trajectory under master–slave mode, which shows that the master–slave motion control is correct.

The master–slave trajectory tracking responses and tracking errors in three directions of Cartesian space are also shown in Fig. 9. The maximum absolute value errors and the root mean square (RMS) errors are given in Table 2.

It can be drawn conclusions from Fig. 9 and Table 2 that the PSM1 with the surgical drill instrument can achieve a good trajectory tracking performance and an intuitive motion control.

5.2 The Calibration Experiment. According to Eq. (13), to obtain the mass and centroid of the drill, and force and torque bias values, the force and torque values and the drill orientation in the world coordinate frame need to be measured when the drill is in free space.

Combined with Eqs. (14) and (15), the mass and centroid of the drill and force and torque bias values can be obtained by applying singular value decomposition (SVD) and the measured values of the F/T sensor in different orientations of the surgical drill instrument in the world coordinate frame. Therefore, $\mathbf{X}_F$ and $\mathbf{X}_\tau$ have solutions of the form

$$\begin{aligned} \mathbf{X}_F &= \mathbf{V}_F \mathbf{S}_F^+ \mathbf{U}_F^T \mathbf{F}_s \\ \mathbf{X}_\tau &= \mathbf{V}_\tau \mathbf{S}_\tau^+ \mathbf{U}_\tau^T \boldsymbol{\tau}_s \end{aligned} \tag{21}$$

where $\mathbf{V}_F$, $\mathbf{S}_F$, $\mathbf{U}_F$ and $\mathbf{V}_\tau$, $\mathbf{S}_\tau$, $\mathbf{U}_\tau$ are the matrices generated by solving the SVD of $\mathbf{Y}_F$ and $\mathbf{Y}_\tau$, respectively, and $\mathbf{S}_F^+$ and $\mathbf{S}_\tau^+$ are the pseudo-inverse matrices of the matrices $\mathbf{S}_F$ and $\mathbf{S}_\tau$, respectively.

For calibration, 2600 sampling values were recorded, with values uniformly distributed throughout the workspace. The first half of the collected data was utilized to calibrate the mass and centroid of the drill and force and torque offset. The second half of the collected data was utilized to evaluate the force and torque calibration results. The calibration results of the mass and centroid of the drill and force and torque offset are given in Table 3.

The force and torque calibration errors after the gravity and force/torque offsets compensation are shown in Fig. 10. Table 4 gives the median and maximum errors of the forces and torques.

It can be known from Fig. 10 and Table 4 that the force and torque calibration errors after gravity and force/torque offsets

Table 4 The median and maximum errors of the forces and torques

	F_x (N)	F_y (N)	F_z (N)	τ_x (N·m)	τ_y (N·m)	τ_z (N·m)
Median	−0.0378	0.0719	−0.0619	0.0009	−0.0011	0.0008
Maximum	0.1143	0.2635	−0.1691	0.0028	−0.0024	0.0013

Table 3 The calibration results

m (kg)	r_x (m)	r_y (m)	r_z (m)	F_{ox} (N)	F_{oy} (N)	F_{oz} (N)	τ_{ox} (N·m)	τ_{oy} (N·m)	τ_{oz} (N·m)
0.0876	0.0010	0.0023	−0.0102	−1.1453	0.5073	−0.7198	0.0029	0.0187	0.0034

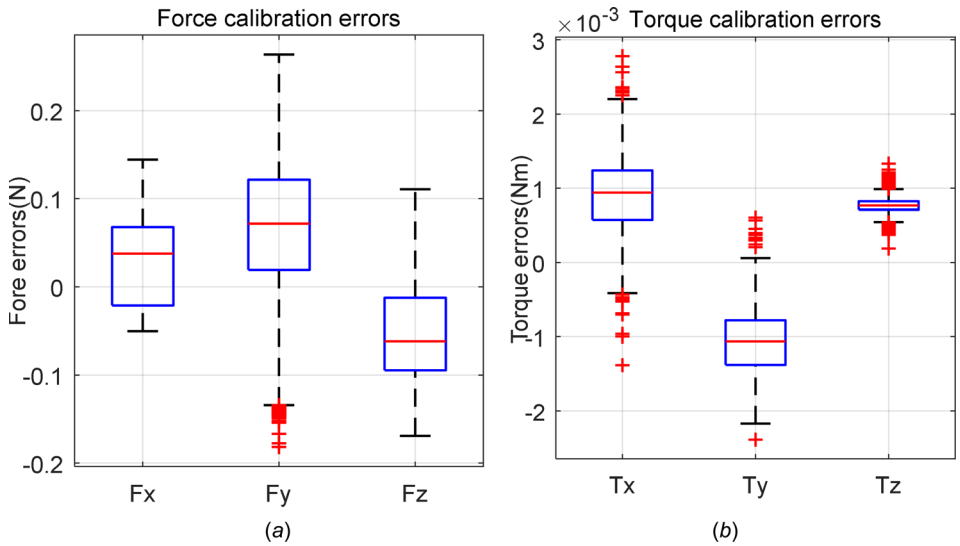

Fig. 10 The calibration errors: (*a*) force errors and (*b*) torque errors

compensation are minor, which can meet the drilling force feedback requirement.

5.3 The Drilling Experiment With Force Feedback. An experimental setup has been developed to perform a drilling experiment with force feedback, as shown in Fig. 6. PHACON temporal bone model was used. The force and the torque between the tip of the burr surgical drill and the bone were measured by the F/T sensor. The force and the torque, transformed and compensated into the control point coordinate frame of the PSM1, was fed back to the MTMR as the body wrench and transformed into joint torque commands at the MTMR. The master–slave force transformation has been verified through each direction in Cartesian space before the drilling experiment is carried out. Reaming

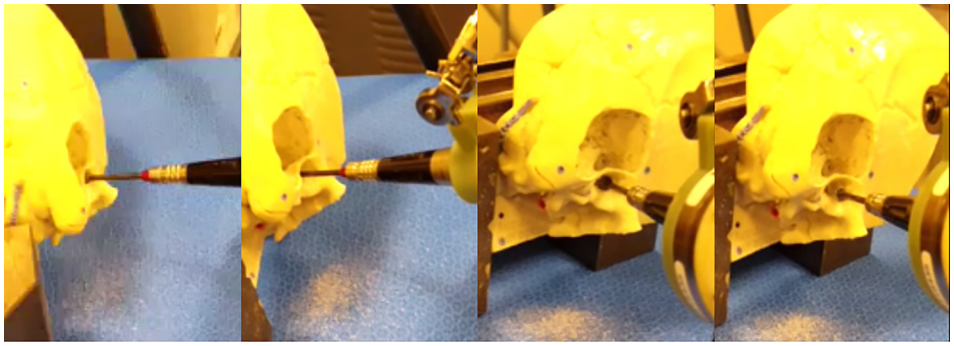

Fig. 11 The process of the reaming: (*a*) start, (*b*) feed, (*c*) back, and (*d*) end

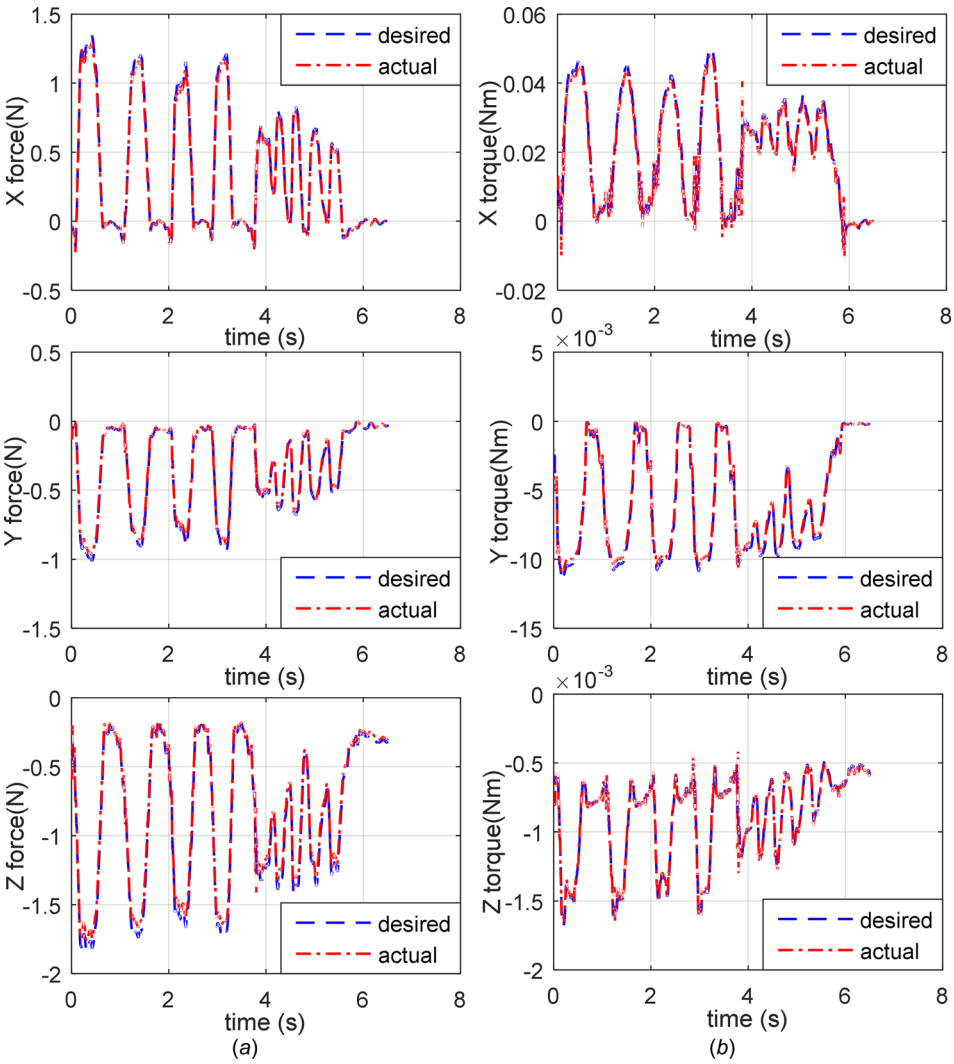

Fig. 12 The force and torque tracking responses of the MTMR: (*a*) force tracking and (*b*) torque tracking

Table 5 The RMS of force and torque tracking errors of the MTMR

	X force (N)	*Y* force (N)	*Z* force (N)	*X* torque (N·m)	*Y* torque (N·m)	*Z* torque (N·m)
RMS	0.0104	0.0065	0. 0125	0.00081	0.00033	0.00029

of the skull model using the drill instrument was implemented under master–slave mode with a motion scale factor of 5:1 and a force scale factor of 1:1. The process of the reaming is shown in Fig. 11.

The force and torque tracking responses of the MTMR are shown in Fig. 12. The actual force and torque are obtained using the actual joint torques and the force Jacobian matrix. Table 5 gives the RMS errors of force and torque tracking of the MTMR.

Figures 11 and 12 and Table 5 showed that the reaming task with force feedback could be successfully completed and the MTMR could provide accurate force and torque tracking performance, which further showed that force transformation was correct.

6 Conclusions

To investigate the feasibility of using a master–slave surgical robotic system to accomplish surgical drilling for otolarngology procedures, a modified da Vinci surgical instrument with force sensing has been developed. The forward kinematics of the PSM1 was analyzed using the modified DH convention. The tooltip-offset transform matrix was obtained by homogenous transformation matrices. The position and the torque coupling matrices between joints and disks of the tendon-driven surgical drill instrument were also derived. The control structure with force feedback based on the dVRK was implemented. The master–slave rotation matrix was derived. To eliminate noncontact force and torque caused by the gravitational and inertial effects, etc., the force and torque transformation matrix was derived. Force and torque transformation from the sensor coordinate frame to the control point coordinate frame was performed to obtain force and torque information of the control point. The force feedback was accomplished.

The trajectory tracking experiments, the calibration experiment, and the drilling experiment with force feedback have been designed and implemented. The results of the trajectory tracking experiments showed that the kinematics of the PSM1 and master–slave motion control were correct, and master–slave trajectory tracking had a good tracking performance. The mass and centroid of the drill and force and torque bias values were obtained by the measured values of the F/T sensor and the orientation of the surgical drill instrument in the world coordinate frame. The calibration results were evaluated and showed that the force and torque calibration errors after gravity and F/T offsets compensation were minor, which could meet the drilling force feedback requirement. The result of the drill experiment with force feedback showed that the drilling task with force feedback could be successfully achieved and there was excellent force and torque tracking performance at the MTMR side.

In conclusion, though our work showed the feasibility of the approach, additional work including evaluating drill performance under different operators and different bones should be done. In addition, the stability and the transparency under force feedback need to be further studied. The mechanical system could also be improved by using a lower weight electric drill. With these additions, a master–slave surgical robot system might be available for bone drilling in the future.

Acknowledgment

This research was partly supported by the National Natural Science Foundation of China (NSFC) (Grant No. 51205287), the Natural Science Foundation of Tianjin (Grant No. 16JCYBJC18400), and internal funding from the Sheikh Zayed Institute, supported by a generous gift from Abu Dhabi. The authors thank Anton Deguet of the Computational Sensing+Robotics Laboratory of Johns Hopkins University for technical assistance.

References

[1] Díaz, I., Gil, J. J., and Louredo, M., 2013, "Bone Drilling Methodology and Tool Based on Position Measurements," Comput. Methods Prog. Biomed., **112**(2), pp. 284–292.
[2] Assadi, M. Z., Du, X., Dalton, J., Henshaw, S., Coulson, C. J., Reid, A. P., Proops, D. W., and Brett, P. N., 2013, "Comparison on Intracochlear Disturbances Between Drilling a Manual and Robotic Cochleostomy," Proc. Inst. Mech. Eng. H, **227**(9), pp. 1002–1008.
[3] Allotta, B., Giacalone, G., and Rinaldi, L., 1997, "A Hand-Held Drilling Tool for Orthopedic Surgery," IEEE/ASME Trans. Mechatronics, **2**(4), pp. 218–229.
[4] Kaburlasos, V. G., and Petridis, V., 2000, "Fuzzy Lattice Neurocomputing (FLN) Models," Neural Networks, **13**(10), pp. 1145–1170.
[5] Allotta, B., Belmonte, F., Bosio, L., and Dario, P., 1996, "Study on a Mechatronic Tool for Drilling in the Osteosynthesis of Long Bones: Tool/Bone Interaction, Modeling and Experiments," Mechatronics, **6**(4), pp. 447–459.
[6] Ong, F. R., and Bouazza-Marouf, K., 1998, "Drilling of Bone: A Robust Automatic Method for the Detection of Drill Bit Break-Through," Proc. Inst. Mech. Eng. H, **212**(3), pp. 209–221.
[7] Brett, P. N., Baker, D. A., Taylor, R., and Griffiths, M. V., 2004, "Controlling the Penetration of Flexible Bone Tissue Using the Stapedotomy Microdrill," Proc. Inst. Mech. Eng., I, **218**(5), pp. 343–351.
[8] Lee, W. Y., Shih, C. L., and Lee, S. T., 2004, "Force Control and Breakthrough Detection of a Bone-Drilling System," IEEE ASME Trans. Mechatronics, **9**(1), pp. 20–29.
[9] Lee, W. Y., and Shih, C. L., 2006, "Control and Breakthrough Detection of a Three Axis Robotic Bone Drilling System," Mechatronics, **16**(2), pp. 73–84.
[10] Wayne, A., 2014, "Depth Controllable and Measurable Medical Driver Devices and Methods of Use," Smart Medical Devices, Inc., Las Vegas, NV, U.S. Patent No. US20140371752A1.
[11] Taylor, R., Du, X., Proops, D., Reid, A., Coulson, C., and Brett, P. N., 2010, "A Sensory Guided Surgical Micro-Drill," Proc. Inst. Mech. Eng. C, **224**(7), pp. 1531–1537.
[12] Balachandran, R., Mitchell, J. E., Blachon, G., Noble, J. H., Dawant, B. M., Fitzpatrick, J. M., and Labadie, R. F., 2010, "Percutaneous Cochlear Implant Drilling Via Customized Frames: An In Vitro Study," Otolaryngol. Head Neck Surg., **142**(3), pp. 421–426.
[13] Labadie, R. F., Balachandran, R., Mitchell, J. E., Noble, J. F., Majdani, O., Haynes, D. S., Benoit, M. L., Dawant, B. M., and Fitzpatrick, J. M., 2010, "Clinical Validation Study of Percutaneous Cochlear Access Using Patient Customized Microstereotactic Frames," Otol. Neurotol., **31**(1), pp. 94–99.
[14] McRackan, T. R., Balachandran, R., Blachon, G. S., Mitchell, J. E., Noble, J. H., Wright, C. G., Fitzpatrick, J. M., Dawant, B. M., and Labadie, R. F., 2013, "Validation of Minimally Invasive, Image-Guided Cochlear Implantation Using Advanced Bionics, Cochlear, and Medel Electrodes in a Cadaver Model," Int. J. Comput. Assisted Radiol. Surg., **8**(6), pp. 989–995.
[15] Warren, F. M., Balachandran, R., Fitzpatrick, J. M., and Labadie, R. F., 2007, "Percutaneous Cochlear Access Using Bone-Mounted, Customized Drill Guides: Demonstration of Concept In Vitro," Otol. Neurotol., **28**(3), pp. 325–329.
[16] Kratchman, L. B., Blachon, G. S., Withrow, T. J., Balachandran, R., and Labadie, R. F., 2011, "Design of a Bone-Attached Parallel Robot for Percutaneous Cochlear Implantation," IEEE Trans. Biomed. Eng., **58**(10), pp. 2904–2910.
[17] Kratchman, L. B., and Fitzpatrick, J. M., 2013, "Robotically-Adjustable Microstereotactic Frames for Image-Guided Neurosurgery," Proc. SPIE, **8671**, p. 86711U.
[18] Labadie, R. F., Balachandran, R., Noble, J. H., Blachon, G. S., Mitchell, I. E., Reda, F. A., Dawant, B. M., and Fitzpatrick, I. M., 2014, "Minimally-Invasive Image-Guided Cochlear Implantation Surgery: First Report of Clinical Implementation," Laryngoscope, **124**(8), pp. 1915–1922.
[19] Labadie, R. F., Choudhury, P., Cetinkaya, E., Balachandran, R., Haynes, D. S., Fenlon, M. R., Jusczyzck, A. S., and Fitzpatrick, I. M., 2005, "Minimally Invasive, Image-Guided, Facial-Recess Approach to the Middle Ear: Demonstration of the Concept of Percutaneous Cochlear Access In Vitro," Otol. Neurotol., **26**(4), pp. 557–562.
[20] Louredo, M., Díaz, I., and Gil, J. J., 2012, "DRIBON: A Mechatronic Bone Drilling Tool," Mechatronics, **22**(8), pp. 1060–1066.
[21] Dillon, N. P., Mitchell, J. E., Zuniga, M. G., Webster, R. J., and Labadie, R. F., 2016, "Design and Thermal Testing of an Automatic Drill Guide for Less Invasive Cochlear Implantation," ASME J. Med. Devices, **10**(2), p. 020923.

[22] Bell, B., Stieger, C., Gerber, N., Arnold, A., Nauer, C., Hamacher, V., Kompis, M., Nolte, L., Caversaccio, M., and Weber, S., 2012, "A Self-Developed and Constructed Robot for Minimally Invasive Cochlear Implantation," Acta Otolaryngol., **132**(4), pp. 355–360.
[23] Dillon, N. P., Balachandranb, R., Dit Falissec, A. M., Wanna, G. B., Labadie, R. F., Withrow, T. J., Fitzpatrick, J. M., and Webster, R. J., III, 2014, "Preliminary Testing of a Compact, Bone-Attached Robot for Otologic Surgery," Proc. SPIE, **9036**, p. 903614.
[24] Danilchenko, A., Toennies, J. L., Balachandran, R., Baron, S., Munske, B., Webster, R. J., III, and Labadie, R. F., 2011, "Robotic Mastoidectomy," Otol. Neurotol., **32**(1), pp. 11–16.
[25] Nguyen, Y., Miroir, M., Kazmitcheff, G., Ferrary, E., Sterkers, O., and Bozorg, A. G., 2012, "From Conception to Application of a Tele-Operated Assistance Robot for Middle Ear Surgery," Surg. Innovation, **19**(3), pp. 241–251.
[26] Dillon, N. P., Balachandran, R., Fitzpatrick, J. M., Michael, S. A., Robert, L. F., George, W. B., Thomas, W. J., and Robert, W. J., 2015, "A Compact, Bone-Attached Robot for Mastoidectomy," ASME J. Med. Devices, **9**(3), p. 031003.
[27] Payne, C. J., and Yang, G. Z., 2014, "Hand-Held Medical Robots," Ann. Biomed. Eng., **42**(8), pp. 1594–1605.
[28] Liu, W. P., Azizian, M., Sorger, J., Taylor, R. H., Reilly, B. K., Cleary, K., and Preciado, D., 2014, "Cadaveric Feasibility Study of da Vinci Si-Assisted Cochlear Implant With Augmented Visual Navigation for Otologic Surgery," Otolaryngol. Head Neck Surg., **140**(3), pp. 208–214.
[29] Vitiello, V., Lee, S. L., Cundy, T. P., and Yang, G. Z., 2013, "Emerging Robotic Platforms for Minimally Invasive Surgery," IEEE Rev. Biomed. Eng., **6**, pp. 111–126.
[30] MacLachlan, R. A., Becker, B. C., Tabarés, J. C., Podnar, G. W., Lobes, L. A., Jr., and Riviere, C. N., 2012, "Micron: An Actively Stabilized Handheld Tool for Microsurgery," IEEE Trans. Rob., **28**(1), pp. 195–212.
[31] Kazanzides, P., Chen, Z., Deguet, A., Fischer, G. S., Taylor, R. H., and Dimaio, S. P., 2014, "An Open-Source Research Kit for the da Vinci® Surgical System," IEEE International Conference on Robotics and Automation (ICRA), Hong Kong, China, May 31–June 7, pp. 6434–6439.
[32] Chen, Z., Deguet, A., Taylor, R., DiMaio, S., Fischer, G., and Kazanzides, P., 2013, "An Open-Source Hardware and Software Platform for Telesurgical Robotics Research," Workshop on Systems and Architecture for Computer Assisted Interventions (MICCAI'13), Nagoya, Japan, Sept. 22–26 pp. 1–10.